Early detection of coronary microvascular dysfunction using machine learning algorithm based on vectorcardiography and cardiodynamicsgram features

Zhao, X., Gong, Y., Zhang, J., Liu, H., Huang, T., Jiang, J., Niu, Y., Xia, L. & Mao, J

DOI 10.1016/j.irbm.2023.100805
ISSN 1959-0318

Publisher: Elsevier

IRBM 44 (2023) 100805

Contents lists available at ScienceDirect

IRBM

journal homepage: www.elsevier.com/locate/irbm

Elsevier Masson France
EM|consulte
www.em-consulte.com

Original Article

Early Detection of Coronary Microvascular Dysfunction Using Machine Learning Algorithm Based on Vectorcardiography and Cardiodynamicsgram Features

Xiaoye Zhao [a,b,c,1], Yinglan Gong [d,1], Jucheng Zhang [e], Haipeng Liu [f], Tianhai Huang [e], Jun Jiang [g], Yanli Niu [h], Ling Xia [i,j,*], Jiandong Mao [b,a,c,*]

[a] School of Instrument Science and Opto-electronic Engineering, Hefei University of Technology, Hefei, Anhui, China
[b] School of Electrical and Information Engineering, North Minzu University, Yinchuan, Ningxia, China
[c] Key Laboratory of Atmospheric Environment Remote Sensing of Ningxia, Yinchuan, Ningxia, China
[d] Institute of Wenzhou, Zhejiang University, Wenzhou, Zhejiang, China
[e] Department of Clinical Engineering, The Second Affiliated Hospital, Zhejiang University School of Medicine, Hangzhou, Zhejiang, China
[f] Research Centre for Intelligent Healthcare, Coventry University, Coventry, United Kingdom
[g] Department of Cardiology, The Second Affiliated Hospital, Zhejiang University School of Medicine, Hangzhou, Zhejiang, China
[h] Department of Surgery, Inner Mongolia Alxa League High-tech Industrial Development Zone General Hospital, Alxa League, Inner Mongolia, China
[i] Key Laboratory for Biomedical Engineering of Ministry of Education, Hangzhou, Zhejiang, China
[j] Institute of Biomedical Engineering, Zhejiang University, Hangzhou, Zhejiang, China

HIGHLIGHTS

- Non-invasive early detection of coronary microvascular dysfunction (CMD).
- Vectorcardiogram (VCG) and cardiodynamicsgram (CDG) features for CMD detection.
- Our proposed multilayer perceptron model: accuracy of 0.904 and sensitivity of 0.925.
- Temporal and spatial features of VCG and CDG are effective indicators of a CMD.

GRAPHICAL ABSTRACT

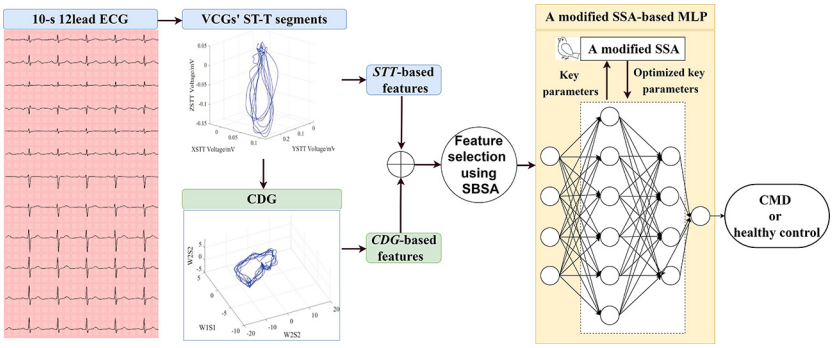

ARTICLE INFO

Article history:
Received 28 October 2022
Received in revised form 24 September 2023
Accepted 25 September 2023
Available online 28 September 2023

Keywords:
Coronary microvascular dysfunction (CMD)
Cardiodynamicsgram (CDG)
Entropy
Sparrow search algorithm (SSA)
Vectorcardiogram (VCG)

ABSTRACT

Purpose: As a main etiology of myocardial ischemia, coronary microvascular dysfunction (CMD) can occur in patients with or without obstructive coronary artery disease. Currently, there is a lack of a non-invasive approach for early detection of CMD.
Aim: We aim to develop a multilayer perceptron (MLP) algorithm to achieve non-invasive early detection of CMD based on vectorcardiography (VCG) and cardiodynamicsgram (CDG) features.
Methods: Electrocardiograms of 82 CMD patients and 107 healthy controls were collected and synthesized into VCGs. The VCGs' ST-T segments were extracted and fed into a deterministic learning algorithm to develop CDGs. Temporal heterogeneity index, spatial heterogeneity index, sample entropy, approximate entropy, and complexity index were extracted from VCGs' ST-T segments and CDGs, entitled as *STT*- and *CDG*-based features, respectively. The most effective feature subsets were determined from *CDG*-based, *STT*-based, and the combined features (i.e., all features) via the sequential backward selection algorithm

* Corresponding authors.
E-mail addresses: xialing@zju.edu.cn (L. Xia), mao_jiandong@163.com (J. Mao).
[1] These authors share first authorship.

https://doi.org/10.1016/j.irbm.2023.100805

Multilayer perceptron (MLP)

as inputs for *CDG*-, *STT*-, and *CDG-STT*-based MLP models optimized with an improved sparrow search algorithm, respectively. Finally, the classification capacity of the corresponding models was evaluated via five-fold cross-validations and tested on a testing dataset to verify the optimal one.

Results: The *CDG-STT*-based MLP model had significantly higher evaluated metrics than *CDG*- and *STT*-based ones on the validation dataset, with the accuracy, sensitivity, specificity, F1 score, and AUC of 0.904, 0.925, 0.870, 0.870, and 0.897 on the testing dataset respectively.

Conclusions: The MLP model based on VCG and CDG features showed high efficiency in identifying CMD. The *CDG-STT*-based MLP model may afford a potential computer-aided tool for non-invasive detection of CMD.

1. Introduction

The coronary arterial system consists the epicardial arteries (diameter $\sim$ 5 mm) and the coronary microvasculature (diameter $<$ 500 μm) which hold 10% and 90% of the total myocardial blood volume, responsible for approximate 25% and 75% of the total coronary vascular resistance for coronary blood flow (CBF), respectively [1]. The abnormality in epicardial arteries or/and coronary microvasculature system can lead to insufficient CBF to meet myocardial metabolic demand, i.e., myocardial ischemia, which has been listed as the leading cause for the global death [2].

Obstructive coronary artery disease (CAD) and coronary microvascular dysfunction (CMD) are two major causes of myocardial ischemia [3]. Obstructive CAD, defined as severe epicardial coronary artery stenosis determined via coronary angiography (CAG, diameter severity [DS] $\geq$ 50%) or a fractional flow reserve (FFR, value $<$ 0.75) [4], has been quantitatively investigated and well established as a main etiology of myocardial ischemia. However, due to the lack of proper tool for microvascular imaging, CMD is not fully understood but has attracted increasing attention. Recently, CMD has been recognized as a main etiology of myocardial ischemia in patients who experience ischemia-like symptoms and signs despite non-obstructive CAD (DS $<$ 50%), (e.g., Cardiac syndrome X), or after the well-established treatment of obstructive CAD [4]. Patients with CMD have higher risks of poor prognosis, rehospitalization, adverse cardiovascular events, and mortality [5,6]. Therefore, the early and accurate detection of CMD is a significant unmet clinical need.

CMD results from the structural or functional abnormalities in coronary microvasculature [7]. CMD disables the coronary microvasculature from dilating to its maximum for increasing CBF to cover an increased myocardial metabolic demand, leading to myocardial ischemia [1,3]. CMD can coexist with CAD [5,6] or occur in the absence of obstructive CAD where the FFR is normal (FFR $\geq$ 0.8) [8–11]. The prevalence of CMD has reported to be 50% to 65% of angina patients with non-obstructive CAD [5], and more than 50% in patients with obstructive CAD, where FFR can locate in the normal range due to the decreased blood flow and pressure drop [9]. Therefore, the diagnostic tools of CAD, including FFR, are not reliable in detecting CMD.

Although a gold standard for coronary microvascular assessment has not yet been established, the index of microcirculatory resistance (IMR) is a well-recognized parameter in diagnosing CMD [3,10,12]. The *in vivo* measurement of IMR is achieved invasively by using an intravascular guide wire with the injection of saline into coronary artery multiple times [13]. Therefore, it is applied only on patients with severe ischemia, and not applicable for the early detection of CMD. Other state-of-the-art techniques including quantitative imaging are not applied in daily clinical practice due to their radiation, high cost, invasiveness, and complicated operation [1]. There is a high need for a non-invasive, accessible, and cost-efficient tool for the early detection of CMD in clinical practice [14].

CMD can lead to ischemic changes in the electrocardiography (ECG) [7,14], which provides the possibility of ECG-based non-invasive detection of CMD. Specially, ischemic ST segment changes [15,16], variations in T wave [14,17], standard deviation of normal R-R intervals [18], and the prolongation of the heart rate-corrected QT interval [17,19] in patients with non-obstructive CAD have been validated as indicators of a CMD. These pilot studies verify the possibility of artificial intelligence algorithms with ECG-based features for detection of CMD. However, due to limited number of CMD-related features and the scarce of data for validation, there is a lack of computer-aided diagnostic tool based on machine learning algorithms. The transformation and in-depth analysis of ECG may disclose more CMD-related features. Vectorcardiogram (VCG), a special type of ECG, could even provide better performance than ECG in detecting myocardial ischemia [20,21]. Some multidimensional VCG features including temporal-heterogeneity index (*THI*), spatial-heterogeneity index (*SHI*), and entropies showed high efficacy in detecting the temporal and spatial changes in VCG signals induced by myocardial ischemia [22]. The cardiac dynamic information underlying VCGs' ST-T segments has been captured for the detection of obstructive CAD via cardiodynamicsgram (CDG) constructed via the deterministic learning algorithm [23]. The shapes of CDGs significantly differ between patients with obstructive CAD (irregular shapes) and healthy controls (regular shapes) [23]. Some patients with ischemic symptoms showed irregular CDGs, but had non-obstructive CAD, where CMD might play a key role. The initial observations in existing studies suggest that temporal and entropy features of VCG and CDG might be used as the indicators of a CMD [22,23]. However, there is a lack of studies on VCG- and CDG-based non-invasive detection of CMD. In this study, we aim to investigate the effectiveness of VCG and CDG features in detecting CMD and develop an optimized machine learning algorithm as the first attempt to fill the gap in patient-specific, non-invasive early detection of CMD.

2. Materials and methods

The schematic diagram of this work is illustrated in Fig. 1. The 10-second ECGs were cleansed and denoised, and then synthesized into VCGs mathematically. VCGs' ST-T segments were extracted by employing a squeeze and regional approach. Subsequently, CDGs were constructed via a deterministic learning algorithm fed with VCGs' ST-T segments. Multidimensional features were extracted from CDGs' and VCGs' ST-T segments, and entitled as *CDG*- and *STT*-based features, respectively. Subsequently, the most effective feature subsets were determined from *CDG*-based, *STT*-based, and the combined features, i.e., all features, by adopting the sequential backward selection algorithm (SBSA), generating *STT*-, *CDG*-, and *STT-CDG*-based multilayer perceptron (MLP) models. The number of neurons in hidden layers of MLP models was optimized with a modified sparrow search algorithm (SSA). Finally, the classification performances of three models were comprehensively evaluated using five-fold cross-validations on a training-validation dataset and

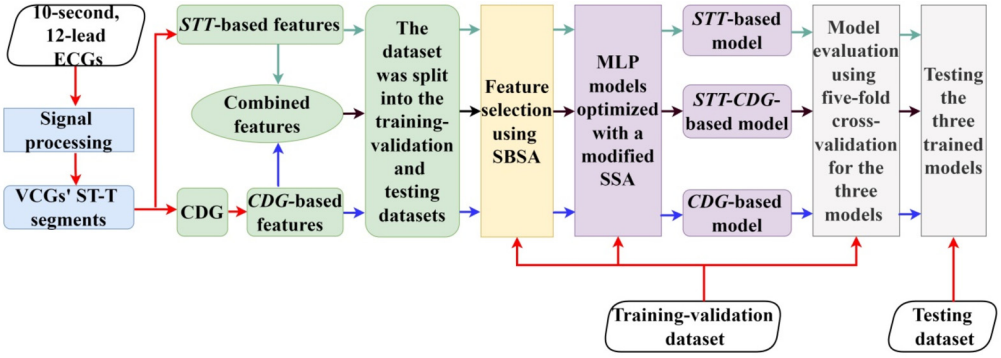

Fig. 1. The schematic diagram of our algorithm. (ECG: electrocardiography, VCG: vectorcardiogram, CDG: cardiodynamicsgram, SBSA: sequential backward selection algorithm, and SSA: sparrow search algorithm.)

tested on a testing dataset to identify the best one for the detection of CMD.

2.1. Data information

In this retrospective study, ECGs and clinical characteristics were collected from 189 subjects of two cohorts. Regarding negative samples, 107 12-lead ECGs (duration: $\geq$ 10 seconds; resolution: 16-bit with 1 μV/LSB; sampling rate: 500 Hz) were obtained from 107 healthy controls (73 females and 34 males, age: 36.3±15.1 years) of China Physiological Signal Challenge 2018 database [24].

As for positive samples, CMD was diagnosed according to standardized diagnostic criteria proposed by COVADIS (Coronary Vasomotor Disorders International Study Group): IMR $\geq$ 25 and FFR $>$ 0.8 [10,25]. FFR and IMR were measured in a standard fashion by employing a coronary guidewire (St. Jude Medical Inc., PressureWireCertus, C12008) during maximal hyperemia [25].

Inclusion criteria applied to positive samples were given by: (1) absence of epicardial flow-limiting stenosis (FFR $\geq$ 0.8); (2) existence of stable or chronic symptoms of myocardial ischemia; (3) presence of symptoms of chest pain or tightness but no obvious evidence of myocardial ischemia; or (4) presence of objective evidence of myocardial ischemia.

Exclusion criteria for positive samples were described as follows: (1) existence of unsuccessful measurement of FFR or IMR; (2) myocardial infarction occurred within 72 hours after measurement; or (3) existence of the following comorbidities: atrial fibrillation, left ventricular hypertrophy, bundle branch blocks, congestive heart failure, pulmonary arterial hypertension, or heart valve disease.

All the existing cases with FFR and IMR measurements up to December 2022 were comprehensively reviewed in the Second Affiliated Hospital of Zhejiang University with approval from local ethics committee for sharing and analyzing retrospective anonymised patient data. Eventually, 82 patients with CMD and their 118 10-second, 12-lead ECGs (sampling rate: 500 Hz; resolution: 16-bit with 5 μV/LSB) recorded utilizing a commercially available electrocardiograph (Netherlands Philips Electronics Co. LTD, PageWriter TC30) were chosen. The local ethics committee waived the requirement of written informed consent for participation. The clinical characteristics of patients with CMD are listed in Table 1.

Table 1
Clinical characteristics of patients with CMD.

Parameter	Values*
Basic characteristics	
Age, years	67.41±8.99
Female, n (%)	34 (46.34)
Heart rate, bpm	72.00±13.13
Systolic blood pressure, mmHg	132.17±17.16
Diastolic blood Pressure, mmHg	73.47±10.35
Risk factors	
Smoking history, n (%)	19 (23.17)
Hypertension, n (%)	44 (53.65)
Diabetes mellitus, n (%)	28 (34.15)

* Quantitative and count variables are shown in mean ± standard deviation, and number (percentage %), respectively.

2.2. Signal preprocessing

After ECGs were cleansed, ECGs from healthy controls were segmented into 10-second segments. 319 10-second, 12-lead ECGs (201 from healthy controls, 118 from CMD patients) were finally selected for further analysis. On the selected ECG segments, the baseline drift and low-frequency fluctuations ($<$ 0.5 Hz) were eliminated via two moving median filters connected in cascade (with length 1.2 and 0.6 seconds respectively) [23] to maximally avoid the deformation of ST segment in comparison with the classical high-pass filter. High-frequency power-line interference and electromyogram noise (10-230 Hz) were eliminated via discrete wavelet transform (DWT)-based filtering algorithm, which can be found in [22].

The VCG consists of three orthonormal leads (leads V_x, V_y, and V_z) [21,26] which represent cardiac electric activity in the frontal, horizontal, and sagittal planes [27]. VCG reflects both the magnitude and spatial information of heart activity in comparison with 12-lead ECG (leads I, II, III, avR, avL, avF, V1, V2, V3, V4, V5, and V6) [28]. The VCGs can be synthesized from 12-lead ECGs [29], as exemplified in Equation (1).

$$\begin{bmatrix} V_x \\ V_y \\ V_z \end{bmatrix} = \begin{bmatrix} 0.38 & -0.07 & -0.13 & 0.05 & -0.01 & 0.14 & 0.06 & 0.54 \\ -0.07 & 0.93 & 0.06 & -0.02 & -0.05 & 0.06 & -0.17 & 0.13 \\ 0.11 & -0.23 & -0.43 & -0.06 & -0.14 & -0.20 & -0.11 & 0.31 \end{bmatrix} \cdot \begin{bmatrix} I \\ II \\ V1 \\ V2 \\ V3 \\ V4 \\ V5 \\ V6 \end{bmatrix} \quad (1)$$

where V_x, V_y, and V_z are the digital voltage values sampled from the corresponding leads of VCG. I, II, $V1$, $V2$, $V3$, $V4$, $V5$, and $V6$ present the digital voltage values sampled from the corresponding leads of ECG.

Ultimately, ST-wave onsets were determined on the VCGs utilizing a squeeze algorithm, and T-wave offsets employing a regional approach to obtain ST-T segments for feature extraction [30].

2.3. Feature extraction

2.3.1. STT-based features

The time series of each VCG lead was obtained by splicing the corresponding ST-T segments beat by beat and contained about 900 to 1200 points, each of which presented digital voltage value sampled during ST-T duration. The time series in all VCG leads formed VCGs' three-dimensional (3-D) ST-T loops. *SHI* and *THI* were calculated from VCGs' 3-D ST-T loops to evaluate CMD-related spatial and temporal characteristics using Equations (a.1) and (a.2) in the *Supplementary Material*, and entitled as *VCGSHI* and *VCGTHI* respectively.

Each time series was standardized to have its standard deviation be one. For each VCG lead, sample entropy (*SampEn*), approximate entropy (*ApEn*), and complexity index (CI) were calculated from the standardized time series to measure the complexity of beat-to-beat ST-T segment employing Equations (a.3), (a.4), and (a.5) in the *Supplementary Material*, and entitled as $V_iSampEn$, V_iApEn, and V_iCI, $i = x, y, z$.

2.3.2. CDG calculation

The deterministic learning algorithm can accurately model the dynamics of the system that generates periodic trajectories, and represent it in a time-invariant manner. The VCGs are non-stationary periodic trajectories generated from the heart moving periodically in 3-D space in cardiac cycles (Fig. 2a-b). Therefore, the dynamics underlying VCG' ST-T segments (Fig. 2c-d) can be modeled via the deterministic learning algorithm and presented as CDG [23].

CDG could be presented as: $\dot{V}_{stt} = F(v_{stt}, \eta) = [f_1(v_{xstt}(t)), f_2(v_{ystt}(t)), f_3(v_{ystt}(t))], V_{stt}(t_0) = v_0$, where $V_{stt} = \left[v_{xstt}, v_{ystt}, v_{zstt}\right]$ represents VCGs' ST-T segments, $F(V_{stt}; \eta)$ is a nonlinear function vector and presents the cardiac dynamics underlying the ST-T segments, and η is a constant vector of system parameters.

In the deterministic learning algorithm, three localized Radial Basis Function (RBF) neural networks were constructed to approximate the cardiac dynamics, i.e., $F(V_{stt}; \eta)$.

$$\dot{\hat{V}}_{stt} = -A(\hat{V}_{stt} - V_{stt}) + \hat{\omega}^T S(V_{stt}) \tag{2}$$

where $\hat{V}_{stt} = \left[\hat{v}_{xstt}, \hat{v}_{ystt}, \hat{v}_{zstt}\right]$ is the state vector of dynamic RBF neural network, A is constant matrix with all entries greater than zero, and $\hat{\omega}$ represents the approximate value of the optimal weight. $S_i(V_{stt}) = [s_{i1}(V_{stt} - \zeta_1), \ldots, s_{iN}(V_{stt} - \zeta_N)]$ is radial basis function, $s_{ij}(\cdot)$ is Gaussian function, and ζ_i is distinct points in state space.

$\dot{\hat{\omega}}$ was updated as follows:

$$\dot{\hat{\omega}} = \dot{\tilde{\omega}} = -\Gamma S(V_{stt})\tilde{V}_{stt} - \delta\Gamma\hat{\omega} \tag{3}$$

where $\tilde{V}_{stt} = \hat{V}_{stt} - V_{stt}$, $\Gamma_i = \Gamma_i^T > 0$, $\tilde{\omega} = \hat{\omega} - \omega^*$, ω^* represents the optimal weight, and δ is a constant with small value.

By using three RBF neural networks $\hat{\omega}_i^T S_i(V_{stt})$, $i = 1, 2, 3$ with an initial weight, $\hat{\omega}_i(0) = 0$, the outputs of RBF neural networks are the approximation of $F(V_{stt}; \eta)$ according to Equation (4). Accordingly, CDG is drawn as the 3-D graphic representation of the information (Fig. 2e-f).

$$\begin{aligned} F(V_{stt}; \eta) &= \bar{\omega}^T S(V_{stt}) + err(V_{stt}) \\ &\approx \left[\bar{\omega}_1^T S_1(v_{xstt}), \bar{\omega}_2^T S_2(v_{ystt}), \bar{\omega}_3^T S_3(v_{zstt})\right] \\ &= [W_1S_1, W_2S_2, W_3S_3] \end{aligned} \tag{4}$$

where $\bar{\omega}$ represent the arithmetic mean of the value of $\hat{\omega}$, and err are the practical approximation errors.

2.3.3. CDG-based features

CDGSHI and *CDGTHI* were calculated from CDG employing Equations (a.1) and (a.2) in the *Supplementary Material*. After W_iS_i, $i = 1, 2, 3$ was standardized to have its standard deviation be one, $W_iS_iSampEn$, W_iS_iApEn, and W_iS_iCI were calculated employing Equations (a.3), (a.4), and (a.5) in the *Supplementary Material* respectively.

2.4. Feature selection

SBSA [31] was implemented to identify the most effective feature subset as the input of MLP models for distinguishing CMD patients and healthy controls. First, a collection of candidate feature subset was created on the training-validation dataset. Specially, the iteration variable n was initially set to be the number of initial features. Each subset with $n - 1$ features was trained and evaluated to select the candidate one with the highest five-fold cross-validation F1 score as the input of next iteration where the subsets with $n - 2$ features derived from the selected $n - 1$ element subset were evaluated and compared similarly. The iteration continued until $n = 1$. Finally, the optimal feature subset with the maximal five-fold cross-validation F1 score was selected from the SBSA-generated candidate feature subsets in the iterations.

2.5. CMD detection using MLP models optimized with the modified SSA

2.5.1. MLP model design

Class-imbalance ratio is proposed to evaluate the extent of class-imbalance which is a common concern in medical datasets [32]. When the class-imbalance ratio is less than 1:9, MLP shows high robustness against class-imbalance on real world benchmark data [33,34]. In current study, the class-imbalance ratio between CMD patients and healthy controls was 1:1.30, which is much lower than the threshold value of 1:9 and fully applicable for the development of MLP models.

MLP model is a particular case of supervised Artificial Neural Network, where each neuron of the architecture implements a logistic function and has an input layer, several hidden layers, and an output layer. For the model design, *CDG*- and *STT*-based model denoted MLP framework fed with *CDG*- and *STT*-based features, respectively. Meanwhile, *CDG-STT*-based model included both *CDG*- and *STT*-based features as inputs. MLP models with two hidden layers were generated using Python 3.7 employing an open-source library Scikit-learn (http://scikit-learn.org/stable) to distinguish between healthy controls and CMD patients.

2.5.2. Hyper-parameters optimization using the modified SSA

Determining the network topology is one of the important aspects of MLP. The number of neurons in the input and output layers are determined by the number of the inputs and outputs respectively [35]. The number of neurons in the hidden layer, referred to as hyper-parameters of MLP model [36] plays an important role for the classification performance and should be determined before the training, given that it cannot be learned during the training process [37,38]. Previous studied has used swarm optimization algorithms to determine the number of neurons in the hidden layer of MLP model [39,40].

SSA, a novel swarm intelligence optimization algorithm, was utilized to optimize the number of neurons in hidden layers of MLP model because of its stronger optimization ability and faster convergence speed compared with other swarm optimization algorithms [41].

Whereas, two major problems make SSA easy to be trapped into local optimal solutions, leading to premature convergence. Firstly, the initialization strategy of the basic SSA is a simple random

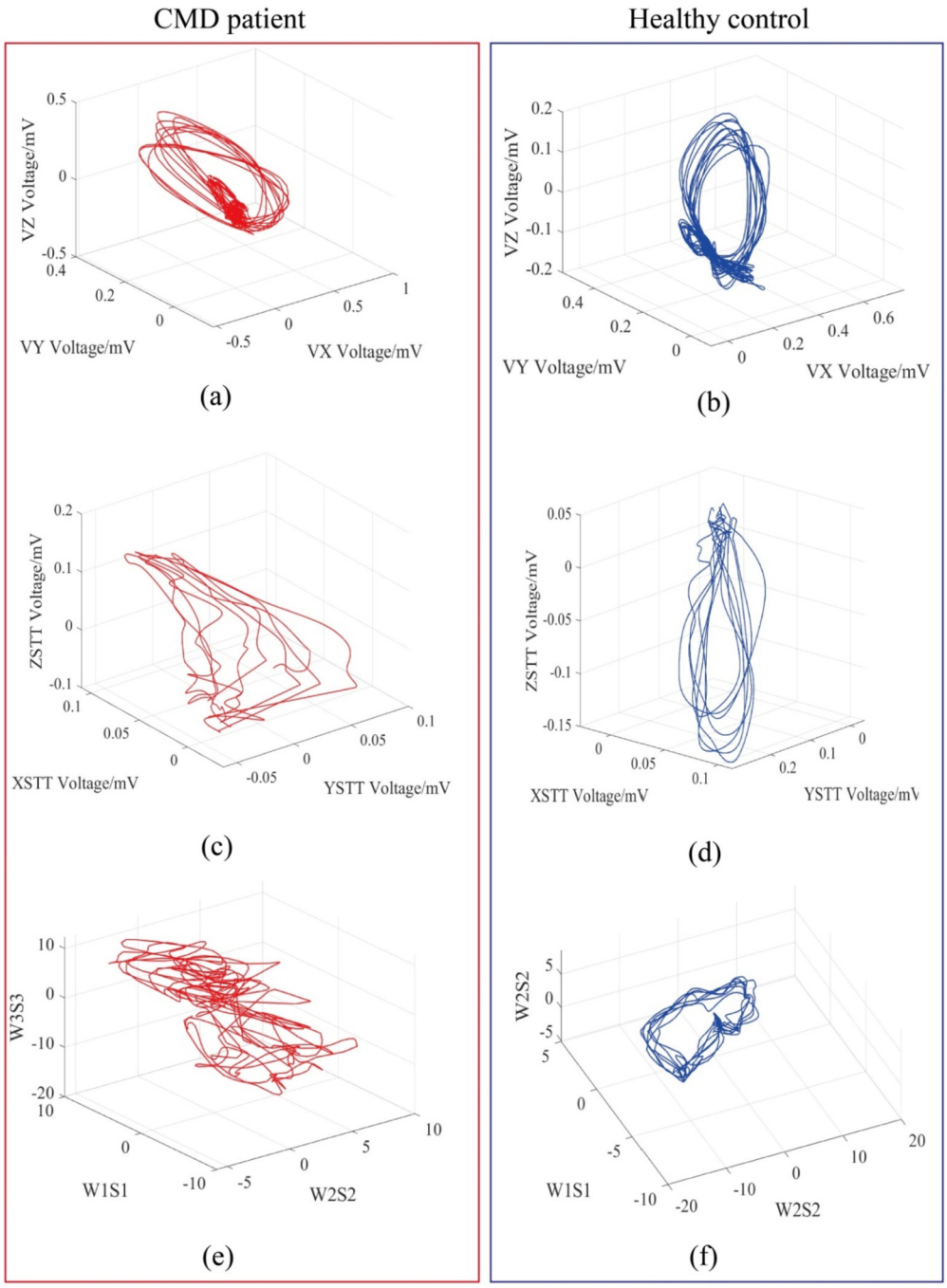

Fig. 2. VCG, VCG's ST-T loops, and CDG. (a) 10-second VCG from a CMD patient. (b) 10-second VCG from a healthy control. (c) VCG's ST-T loops from a CMD patient. (d) VCG's ST-T loops from a healthy control. (e) CDG from a CMD patient. (f) CDG from a healthy control.

method, making the performance of the algorithm largely dependent on the diversity of the initial populations [42,43]. Secondly, the sparrow group gradually clusters around the local optimal position and has poor population diversity in later iterations, which can induce a local aggregation in the optimization process [44]. To overcome these limitations, we proposed a modified SSA integrating chaotic map and Gaussian mutation [45] bespoke for the hyper-parameters (i.e., the numbers of neurons in the hidden layer one and two) optimization (Fig. 3).

SSA simulates the sparrow's foraging process, and the sparrow population consists of the discoverers, participants, and watchmen. A discoverer with better fitness value guides the population towards the area with food. The participants obey the discoverers' guidance and find food. The identity of the discoverers and the participants is not fixed, and they can convert into each other. The watchmen warn of environmental threats and decide whether the population moves closer to a much safer area.

The position of the *ith* sparrow was set to be $P_i = [p_{i1}, \cdots, p_{ij}, \cdots, p_{iD}]$, $i = 1, 2, \ldots, N$, where p_{ij} represents the position of the *ith* sparrow in the *jth* dimension. N and D are the number of sparrows and the dimension of the parameters to be optimized.

To overcome the limitations of random initialization strategy of SSA, the chaotic variables were calculated using the Bernoulli chaotic map in our algorithm [46] to increase the diversity of initial positions and enhance the global search ability of the algorithm as follows:

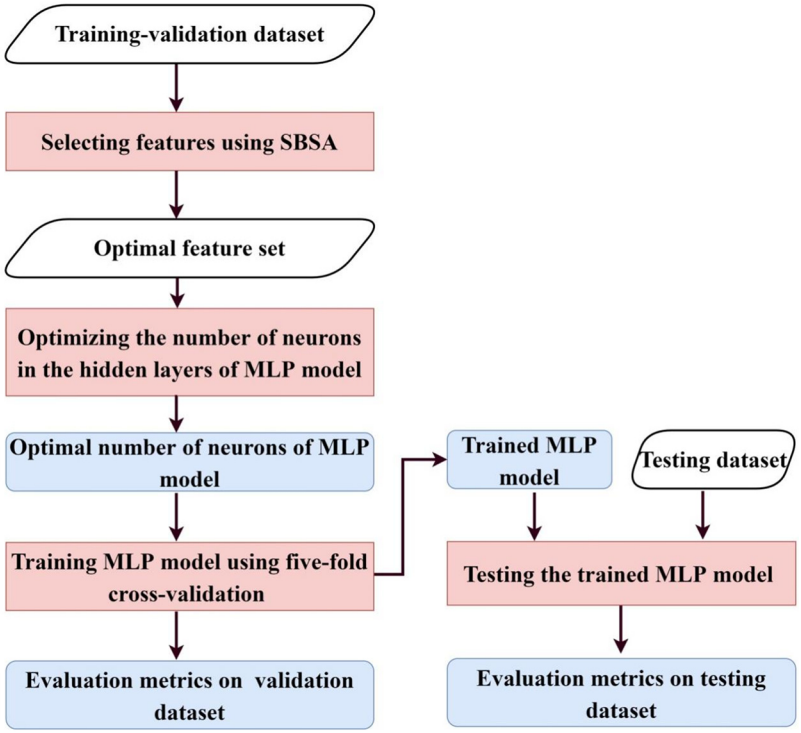

Fig. 3. The flowchart of MLP models optimized with the modified SSA. (MLP: multilayer perceptron, SBSA: sequential backward selection algorithm, and SSA: sparrow search algorithm.)

$$b_{i+1j} = \begin{cases} \frac{b_{ij}}{(1-\lambda)}, & b_{ij} \in (0, 1-\lambda] \\ \frac{(b_{ij}-1+\lambda)}{\lambda}, & b_{ij} \in (1-\lambda, 1) \end{cases}, \quad i = 1, ..., N, \ j = 1, ..., D \tag{5}$$

where $\lambda = 0.4$ [46].

Then, the chaotic variables were transferred to the solution space of the problem to be solved as follows:

$$p_{ij} = p_{\min} + (p_{\max} - p_{\min}) \times b_{ij} \tag{6}$$

where $p_{\min}$ and $p_{\max}$ present the minimum and maximum values of the parameter to be optimized.

Subsequently, the corresponding fitness function of the *ith* sparrow was based on Equation (7), and the minimum fitness value was taken as the goal. Better classification performance of the algorithm leads to higher $F1$ *score* and lower fitness value.

$$fun(P_i) = 1 - F1\ score \tag{7}$$

where $F1$ *score* denotes F1 score of the MLP model on the training-validation dataset. $F1$ *score* takes into account precision and recall, and is not sensitive to the class-imbalance [47].

In each iteration step, the position of the discoverer was updated as follows:

$$p_{ij}^{t+1} = \begin{cases} p_{ij}^{t} \cdot \exp(-\frac{i}{rand(0,1) \cdot iter_{\max}}), & R_2 < ST \\ p_{ij}^{t} + Q \cdot L, & R_2 \geq ST \end{cases} \tag{8}$$

where t is the current iteration time, and $iter_{\max}$ represents the maximum number of iterations. $rand(0, 1) \in [0, 1]$ is a random number. Q refers to a standard normal distributed random number. $R_2 \in [0, 1]$ denotes the warning value, and $ST \in [0.5, 1]$ presents the security threshold.

The position of the participant was updated according to the following equation.

$$p_{ij}^{t+1} = \begin{cases} Q \cdot \exp(\frac{p_{worst}^{t} - p_{ij}^{t}}{i^2}), & i > N/2 \\ p_{b}^{t+1} + \left| p_{ij}^{t} - p_{b}^{t+1} \right| \cdot A^{+} \cdot R, & i \leq N/2 \end{cases} \tag{9}$$

where p_{worst}^{t} denotes the current global worst position in response to the highest fitness value, and p_{b}^{t+1} is the optimal position occupied by the discoverer in the $(t+1)th$ iteration. A is a $1 \times D$ matrix with each factor randomly assigned 1 or -1 only, where $A^{+} = A^{T}(AA^{T})^{-1}$. R is a unit row vector of D columns.

The watchman updated its position as follows:

$$p_{ij}^{t+1} = \begin{cases} p_{best}^{t} + N(0,1) \cdot \left| p_{ij}^{t} - p_{best}^{t} \right|, & fun(P_i) > fun_{best} \\ p_{ij}^{t} + K \cdot \left(\frac{\left| p_{ij}^{t} - p_{worst}^{t} \right|}{(fun(P_i) - fun_{worst}) + \gamma} \right), & fun(P_i) = fun_{best} \end{cases} \tag{10}$$

where p_{best}^{t} is the current global optimal position in response to the lowest fitness value. $N(0, 1)$ is a standard normal distributed random number. $K \in [-1, 1]$ is a random number. fun_{best} and fun_{worst} are globally minimal and maximal fitness values in current iteration. γ is a very small constant to avoid the denominator from being zero.

To prevent the sparrow group from clustering around the local optimal position in SSA, Gaussian mutation or Bernoulli chaotic variables were adopted after the first iteration to update the position of sparrows via comparing individual fitness value and the average fitness value, i.e., fun_{avg} of all sparrows [45]. When $fun(P_i) < fun_{avg}$, meaning that the algorithm started clustering, the position of *ith* sparrow was calculated using Gaussian mutation to avoid its position from being clustered as Equation (11) and its fitness value was calculated.

$$p_{ijafter} = p_{ij} \cdot (1 + N(0, 1)) \tag{11}$$

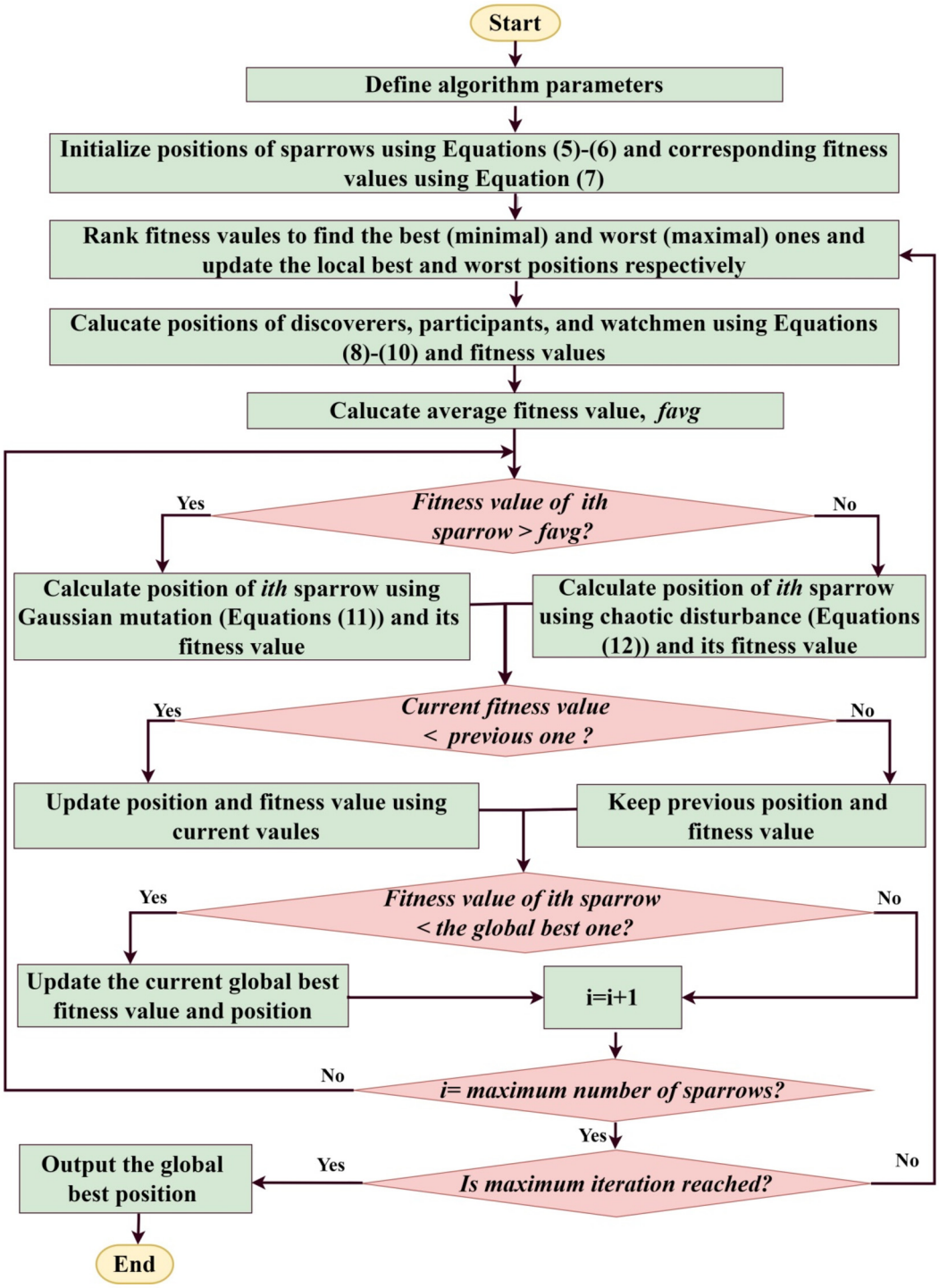

Fig. 4. The flowchart of a modified SSA for the hyper-parameters optimization.

where $p_{ijafter}$ presents the position of the *ith* sparrow calculated using Gaussian mutation or Bernoulli chaotic variables.

When $fun(P_i) \geq fun_{avg}$, meaning that the position of sparrow becomes dispersive, chaotic disturbance was performed to prevent the position of *ith* sparrow from being dispersive as Equation (12), and its fitness value was updated.

$$P_{ijafter} = p_{ij} \cdot (1 + p_{ijnew} \cdot \frac{1}{N_T})/2 \tag{12}$$

where N_T is the number of p_{ij} among all sparrows. p_{ijnew} is the new position updated based on Equations (5)–(6).

The new fitness value of each sparrow was compared with the previous one calculated before Gaussian mutation or Bernoulli chaotic variables. The lower one was accepted with its corresponding position updated simultaneously. The current global optimal position, $p^t_{best,j}$, and its fitness value, fun_{best}, were updated as well as the current global worst position, $p^t_{worst,j}$, and its fitness value, fun_{worst}, for the next iteration.

Finally, the position with the minimal fitness value was found as the optimal hyper-parameters and output to the MLP model. The process of the modified SSA is illustrated in Fig. 4.

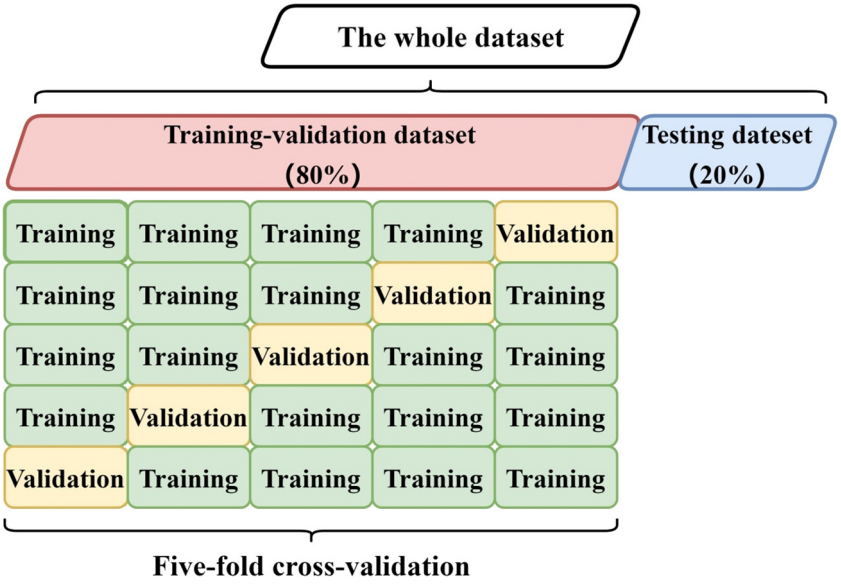

Fig. 5. The dataset split for five-fold cross-validation.

The values of N, D, and $iter_{\max}$ were set to be 30, 2, and 60, respectively. The number of the discoverers and watchmen account for 20% and 10%, respectively, and $ST = 0.8$.

2.6. Experiment and model evaluation

Each subject in positive and negative samples was assigned a unique numeric number, and his/her 10-second ECGs were named and ranked in accordance with his/her numeric number. In general, the first 80% ECGs were split for the training-validation dataset, and the last 20% for the testing dataset [48] (Fig. 5). Near the cut-off point, the ECGs originating from the same patient might be split into the both datasets, which might lead to inaccurate classification performance. To solve this problem, these ECGs were removed into one dataset only manually to ensure the independence of the testing dataset from the train-validation ones. Regard to positive samples, there were 95 ECGs on the training-validation dataset and 23 ones on the testing dataset. As for negative samples, the training-validation dataset contained 161 ECGs and the testing dataset had 40 ones.

A five-fold cross-validation method was adopted for evaluating the classification performance of the constructed models on the training-validation dataset (Fig. 5). Then, the trained model with hyper-parameters optimized by the modified SSA was tested on the testing dataset.

The evaluation metrics consist of accuracy, specificity, sensitivity, F1 score, and the area under the curve (AUC) of the receiver operating characteristic curve [22,49]. AUC of the five-fold cross-validation was used to adjust hyper-parameters of the MLP model [50].

The categorical data were provided as numbers and percentages, and numerical variables as mean ± standard deviation or median with interquartile range according to their distributions, which were checked by utilizing the Kolmogorov-Smirnov test [51]. Our extracted features between healthy controls and CMD patients were compared via independent *t-test* (for normal distribution) or Mann-Whitney U test [52] (for non-normal distribution), and evaluation metrics between different models by using paired t test (for normal distribution) or Wilcoxon signed-sum test (for non-normal distribution). Statistical significance was defined as: $p \leq 0.05$ [53]. The statistical analysis was deployed on SPSS (Version 25.0, IBM Corp).

3. Results

3.1. The results of feature extraction

Fig. 6 shows the *STT*-based features extracted from healthy controls and CMD patients. Compared with healthy controls, patients with CMD afford significantly higher *VCGSHI* (Fig. 6a), *VCGTHI* (Fig. 6b), V_xCI, $V_ySampEn$, V_yApEn, $V_zSampEn$, and V_zCI (Fig. 6c), but lower V_xApEn (Fig. 6c).

The values of features extracted from CDGs are illustrated in Fig. 7. Healthy controls have higher *VCGSHI* than CMD patients (Fig. 7a). It is obvious that the remaining features from patients with CMD are significantly higher than those of healthy controls (Fig. 7b-c).

3.2. Performance evaluation between CDG-STT-based, STT-based, and CDG -based models

The performances of the three models, i.e., *CDG-STT*-based, *STT*-based, and *CDG*-based models on the training dataset are listed in Table 2. That *CDG-STT*-based model outperforms the other two models across all evaluation metrics.

There were significantly differences in accuracy ($P = 0.012$) across the *CDG-STT*-, *CDG*-, and *STT*- models as well as sensitivity ($P = 0.012$), F1 score ($P = 0.009$), and AUC ($P = 0.046$). Fig. 8 illustrates the comparisons of evaluation metrics on the validation dataset between *CDG-STT*- and *CDG*-based models, between *CDG-STT*- and *STT*-based models. As a result, the *CDG-STT*-based model shows significantly better performance than *CDG*-based one in accuracy, F1 score, and AUC. In addition, this model affords significantly higher accuracy and sensitivity than *STT*-based one. Hence, *CDG-STT*-based model was determined as the optimal one for detecting CMD.

The comparisons of the classification performance of the three models on the testing dataset indicated the same trend, as listed in Table 3. *CDG-STT*-based model outperforms both *CDG*- and *STT*-based models across all testing evaluation metrics, with all values higher than 0.8. Specially, the testing accuracy and sensitivity of *CDG-STT*-based model even reaches 0.905 and 0.925 respectively. Hence, *CDG-STT*-based model was verified as the optimal one for the detection of CMD.

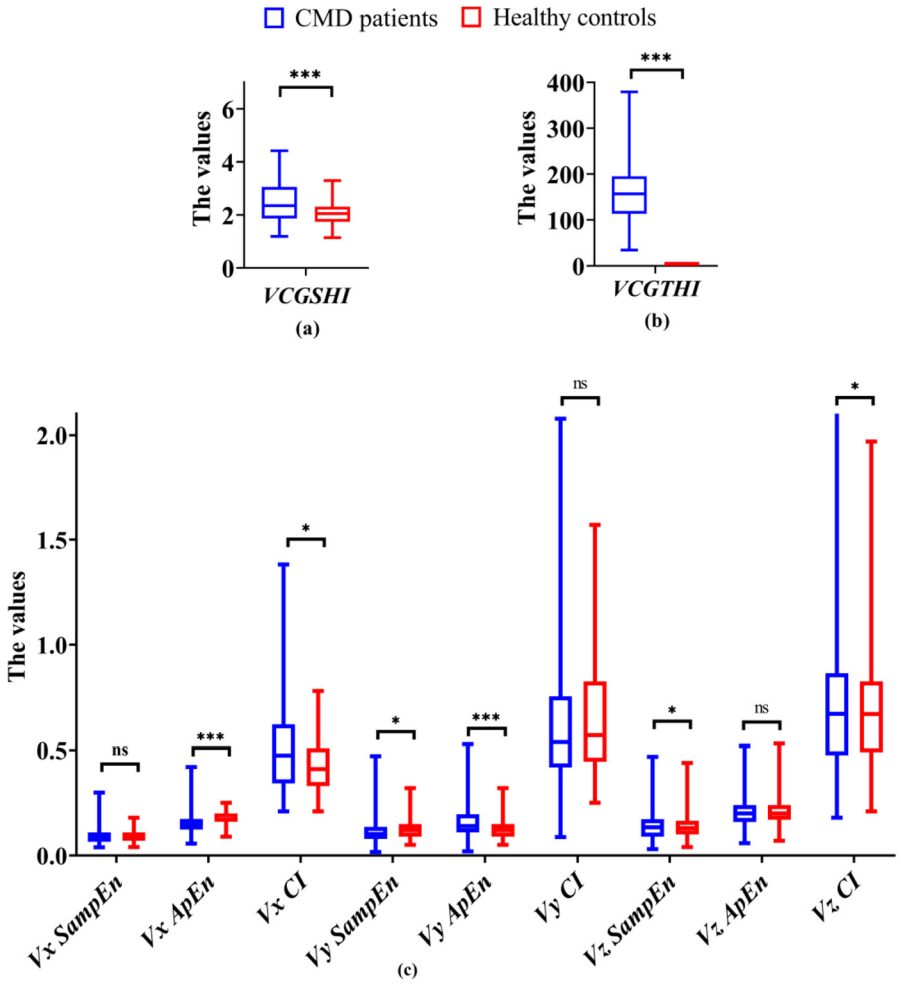

Fig. 6. *STT*-based features values. (a) Values of *VCGSHI*. (b) Values of *VCGTHI*. (c) Values of *SampEn*, *ApEn*, and *CI* extracted from VCGs' ST-T segments. (The *VCG*-based features between two groups were compared via Mann-Whitney U test. ns presents no significance. $^{*}p \leq 0.05$, $^{**}p \leq 0.005$, and $^{***}p \leq 0.001$.)

Table 2
The evaluation metrics of the three models on the training dataset.

Models	Accuracy	Specificity	Sensitivity	F1 score	AUC
CDG-based	0.801±0.027	0.714±0.032	0.850±0.043	0.727±0.024	0.782±0.021
STT-based	0.844±0.059	0.754±0.146	0.907±0.029	0.775±0.068	0.830±0.067
CDG-STT-based	0.967±0.016	0.935±0.044	0.984±0.005	0.893±0.037	0.969±0.022

Table 3
The testing evaluation metrics of the three models.

Models	Accuracy	Specificity	Sensitivity	F1 score	AUC
CDG-based	0.793	0.739	0.825	0.723	0.782
STT-based	0.825	0.696	0.900	0.744	0.798
CDG-STT-based	0.905	0.870	0.925	0.870	0.897

3.3. Comparison of classification performance of CDG-STT-based MLP models optimized with modified SSA and SSA

The *CDG-STT*-based MLPs optimized with modified SSA and SSA are compared on the validation and testing datasets, as listed in Tables 4–5, where the model optimized with modified SSA offers higher evaluation metrics.

4. Discussion

4.1. Comparison with existing studies

Our proposed *CDG-STT*-based MLP model with the hyper-parameters optimized with the modified SSA is validated as the optimal one for the early detection of CMD. With high performance (all testing evaluation metrics over 0.8, specially accuracy of 0.905, sensitivity of 0.925), this algorithm offers the possibility of non-invasive, low-cost early detection of CMD based on the ECG test which is commonly performed in clinical practice.

Obstructive CAD is the leading cause of myocardial ischemia and the focus of previous ECG-based artificial intelligence algorithms of myocardial ischemia detection [54], whereas the investigation on CMD is limited. Recently, standard deviation of normal R-R intervals [18], ischemic ST segment changes [15,16], baseline heart rate-corrected QT interval [19], and variations in T wave [14] have been verified to be indicators of a CMD providing the

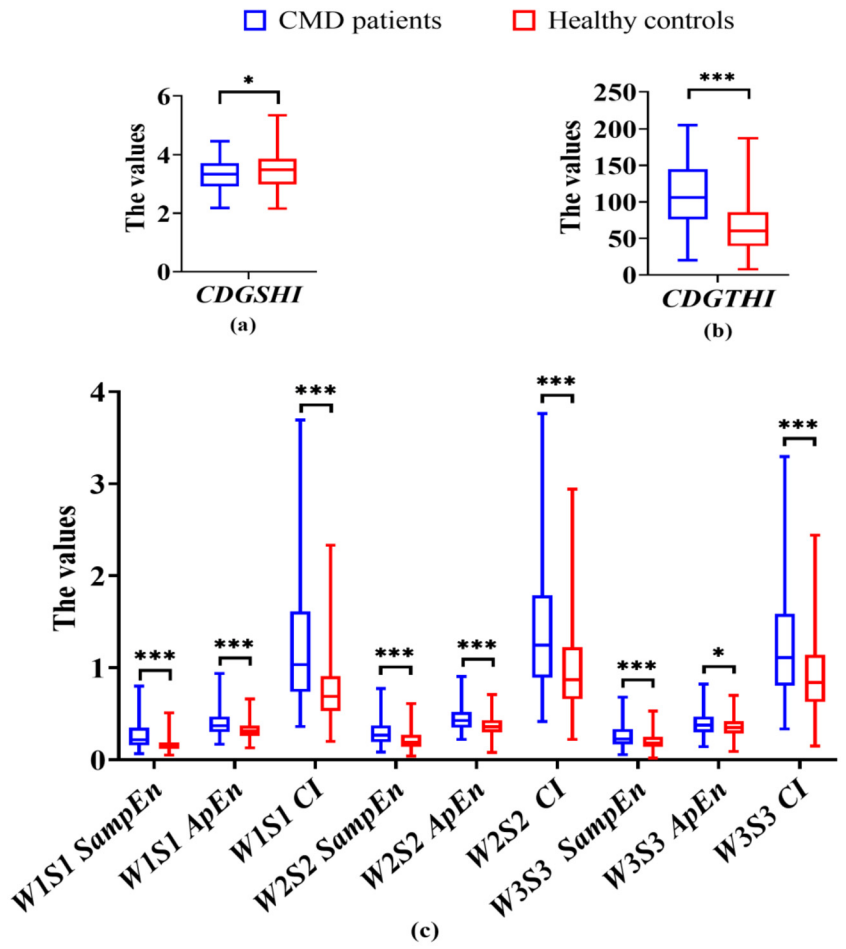

Fig. 7. Values of *CDG*-based features. (a) Values of *CDGSHI*. (b) Values of *CDGTHI*. (c) Values of *SampEn*, *ApEn*, and *C1* extracted from *CDG*. (The *CDG*-based features between two groups were compared via Mann-Whitney U test. ns presents no significance. $^{*}p \leq 0.05$, $^{**}p \leq 0.005$, and $^{***}p \leq 0.001$.)

Table 4
The evaluation metrics on the validation dataset of the CDG-STT-based MLP model optimized with the modified SSA and SSA.

Hyper-parameters optimization method	Accuracy	Specificity	Sensitivity	F1 score	AUC
SSA	0.898±0.054	0.809±0.117	0.945±0.040	0.854±0.081	0.877±0.084
The modified SSA	0.922±0.033	0.876±0.066	0.957±0.027	0.893±0.038	0.916±0.038
P-values	0.084	0.673	0.022*	0.005**	0.130

Note: Data were derived from the five-fold validation.

Table 5
The testing evaluation metrics of the CDG-STT-based MLP model optimized with the modified SSA and SSA.

Hyper-parameters optimization method	Accuracy	Specificity	Sensitivity	F1 score	AUC
SSA	0.841	0.739	0900	0.773	0.820
The modified SSA	0.905	0.870	0.925	0.870	0.897

possibility for ECG-based CMD detection. However, as far as we know, there is a scarcity of computational models for CMD detection. SARA et al. proposed a linear discriminant analysis model with T wave area, T Peak-T end, and Y-center of gravity to detect CMD using coronary flow reserve (CFR) [14]. Their model can identify the existence of an abnormal CFR with the highest accuracy of 66.5 ± 0.3% and 74 ± 2% for females and males, respectively [14]. The authors utilized an abnormal CFR and DS < 50% as the standard for selecting CMD patients to exclude the influence of epicardial coronary artery stenosis. However, the CFR measurement allows for appraisal of the microvasular and epicardial artery function together [6]. In comparison, IMR is directly measured from the distal coronary arteries and has a stronger correlation with the true microcirculatory resistance than CFR [4]. Therefore, we maximally exclude the confounding hemodynamic effect of epicardial stenosis by using IMR as the reference of CMD [1,12]. Additionally, we used FFR as a direct hemodynamic evaluation to exclude CAD patients in positive group.

As far as we known, this is the first attempt on an ECG-based automatic CMD detection algorithm using machine learning models fed with VCG- and CDG-based features. Our proposed model hence can detect CMD in suspicious patients in the absence of

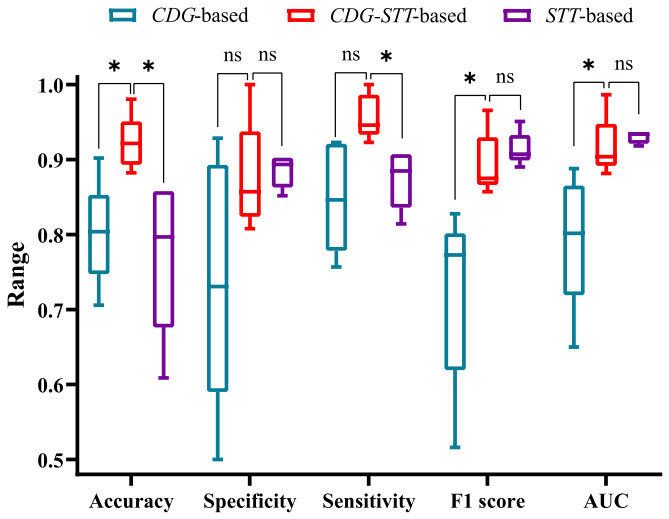

Fig. 8. The comparison of the classification performance of the three models on the validation dataset. (ns presents no significance. $^{*}p \leq 0.05$, $^{**}p \leq 0.005$, $^{***}p \leq 0.001$.)

epicardial flow-limiting stenosis based on resting ECG without any extra exercise.

4.2. Effectiveness of ECG-derived features in detecting CMD

CMD-induced myocardial ischemia can lead to a subtle impairment of repolarization and a heterogeneous repolarization process [1,17], which could be detected from the temporal and spatial properties of the heart vector [55].

VCG represents the trajectory of the tip of the heart vector in three-orthogonal dimensions and records both the direction and magnitude of the heart vector, where CMD-induced repolarization abnormality can be reflected in some variations including altered spatial orientations and magnitude of ST vectors [56,57], T loop morphology, and the T vector angle [58]. Previous studies have indicated that altered T-wave morphology in patients with non-obstructive CAD could be the indicators of a CMD [14,17]. In addition, ST-segment elevation could be used to diagnose microvascular obstruction [15]. In our work, the variations in VCGs' ST-T segments are evaluated using *VCGSHI*, *VCGTHS*, and entropy features, and they are different between healthy controls and patients with CMD (Fig. 6). Therefore, they can be considered as indicators of a CMD.

CDG can present the rate of CAD-induced ischemic ST-T changes in VCG lead and reflect the dynamics on its shapes [23,59]. However, false-positive cases have been reported in detecting CAD using CDG results when DS $\geq$ 50% was determined as the standard for diagnosing ischemia. The coronary slow phenomenon, i.e., the decrease of blood flow in a coronary artery with non-obstructive lesion, was found in the false-positive cases [59]. With these cases (DS $<$ 50% with coronary slow phenomenon) counted as positive, the specificity of CDG-based myocardial ischemia detection increased from 82.6% to 85.2%, which indicated that CMD could be reflected in CDG features [59]. In accordance with the existing observations [23,59], our results revealed that patients with non-obstructive CAD but CMD have irregular CDG compared with healthy controls. The majority of CDG-based features are statistically different between the CMD and control groups (Fig. 7). Integrating *CDG*-based features into *STT*-based ones can significantly improve the classification performance (Fig. 8 and Tables 2–3). Hence, as effective indicators of a CMD, *CDG*-based features deserve further investigation.

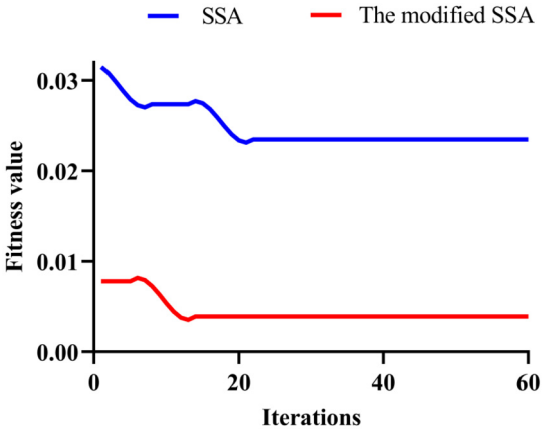

Fig. 9. The fitness values of the modified SSA and SSA in *CDG-STT*-based MLP model.

4.3. Comparison between the modified SSA and SSA

The classification performance of *CDG-STT*-based MLP model optimized with our modified SSA is better than this model optimized with SSA, which means that our modified SSA offered better hyper-parameters than SSA, as listed in Tables 4–5. Then, the fitness values between the modified SSA and SSA in *CDG-STT*-based MLP model are compared in Fig. 9. It can be seen from Fig. 9 that our modified SSA provides lower fitness value and converges faster than SSA. The minimum fitness value of the modified SSA is 0.0039, while that of SSA is 0.0235.

Our proposed modified SSA had two obvious differences from SSA. Firstly, Bernoulli chaotic variables adopted in our algorithm for the generation of the initialized populations are more ergodic and uniform (Fig. 10) than random variables used in SSA [41], which can enhance the randomness of the initial position of sparrows and show higher performance than random method in SSA [42,45,60–62].

Secondly, Gaussian mutation and Bernoulli chaotic variables were carried out in late iterations of SSA to prevent local aggregation in the optimization process and enhance its ability to jump out of local optimization. Gaussian function can randomly produce new solutions around a given position [63], which is beneficial to the algorithm to jump out the local optimum [45,64,65]. Bernoulli chaotic disturbance can decrease positions of sparrows and prevent becomes dispersive [44].

Therefore, the modified SSA can effectively prevent local aggregation in SSA and determine the global optimum efficiently for the optimization problem with a large number of the local optimum [45].

4.4. Strengths, limitations, and future directions

Our study has revealed that features calculated from VCGs' ST-T segments and CDGs could be useful to recognize CMD in the absence of epicardial flow-limiting stenosis. We proposed a modified SSA that can achieve the automatical hyper-parameters optimization of *CDG-STT*-based MLP model. The algorithms could be easily deployed on conventional ECG acquisition equipment and accepted by the physician, given that VCGs and CDGs can be synthesized automatically from standard ECGs with no extra workload for operators. Hence, our results open a new pathway towards non-invasive, low-cost, and operator-friendly detection of CMD in various application scenarios.

However, there are some limitations in our work. First, the number of patients with CMD is smaller than that of healthy controls. The measurements of FFR and IMR are invasive and costly, which is not commonly performed. Therefore, the number of CMD

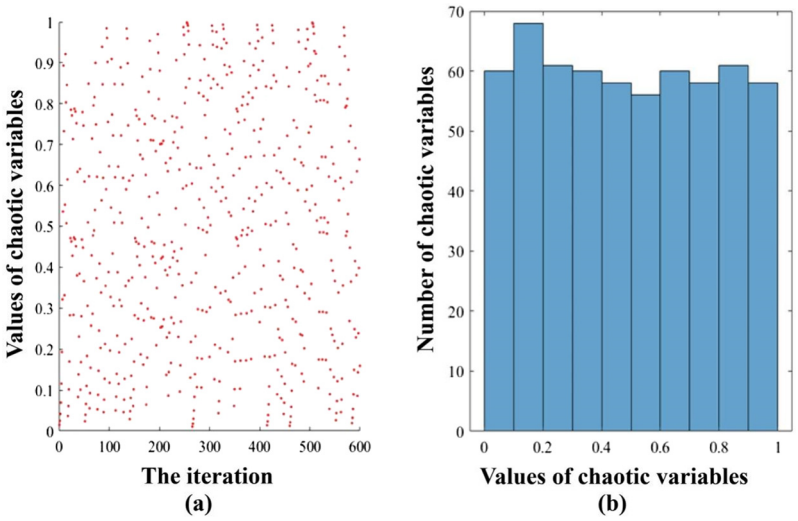

Fig. 10. The distribution of Bernoulli chaotic variables. (a) The chaotic maps. (b) The histogram of chaotic variables.

patients who underwent full examination is limited. Second, the CMD patients are from a single-center cohort. The heterogeneity of physiological conditions is not fully considered. Additionally, the difference in physiological characteristics may influence the classification performance, for patients with CMD and healthy controls were collected from different cohorts. Furthermore, the differentiation between CMD and obstructive CAD was not included in this study but deserves in-depth investigation since they have some similarities in terms of their clinical presentations, laboratory biomarkers, and some ECG features, but their treatment strategies are different. Finally, in this study we focused on ECG-derived features whereas multi-model medical data fusion (e.g., radiological imaging, hematologic tests, and medical history) may enhance the total accuracy of myocardial ischemia diagnosis.

In future studies, multicenter large-scale studies can further validate our results and optimize the algorithm by considering the difference in physiological features. Based on large datasets, the combination of our extracted features with multi-model data fusion (e.g., ultrasonoscopy [66]) could be developed to provide the visible results, improve the classification capability and differentiate between CMD and obstructive CAD.

5. Conclusions

In conclusion, *SampEn*, *ApEn*, *CI*, *THI*, and *SHI* extracted from CDGs' and VCGs' ST-T segments could be effective features to recognize electrocardiographic signatures of CMD. The *CDG-STT*-based MLP model may afford a potential computer-aided tool for non-invasive detection of CMD.

Ethics approval

The study was approved by Ethics committee of the Second Affiliated Hospital of Zhejiang University.

Human and animal rights

The authors declare that the work described has been carried out in accordance with the Declaration of Helsinki of the World Medical Association revised in 2013 for experiments involving humans as well as in accordance with the EU Directive 2010/63/EU for animal experiments.

Informed consent and patient details

The authors declare that this report does not contain any personal information that could lead to the identification of the patient(s).

Funding

This work has been supported by: Natural Science Foundation of Ningxia Province, [grant number 2022AAC03242]; North Minzu University Scientific Research Projects, [grant number 2021JCYJ10]; Natural Science Foundation of China (NSFC) [grant number 62171408]; Major Scientific Project of Zhejiang Laboratory [grant number 2020ND8AD01]; Key Research and Development Program of Zhejiang Province, [grant number 2020C03016]; Ningxia First-Class Discipline and Scientific Research Projects (Electronic Science and Technology) [grant number NXYLXK2017A07]; Plan for Leading Talents of the State Ethnic Affairs Commission of the People's Republic of China; Innovation Team of Lidar Atmosphere Remote Sensing of Ningxia Province; High Level Talent Selection and Training Plan of North Minzu University; Key Research and Development Plan in Ningxia Province, [grant number 2023BEG02065]; Sub-themes of Key and Major Special Projects of Scientific and Technological Innovation of Yinchuan Science and Technology Plan Project, [grant number 2021-SF-009].

Author contributions

All authors attest that they meet the current International Committee of Medical Journal Editors (ICMJE) criteria for Authorship.

CRediT authorship contribution statement

Xiaoye Zhao: Funding acquisition, Methodology, Software, Writing – original draft. **Yinglan Gong:** Project administration, Software, Validation. **Jucheng Zhang:** Resources. **Haipeng Liu:** Writing – review & editing. **Tianhai Huang:** Resources. **Jun Jiang:** Data curation, Funding acquisition. **Yanli Niu:** Validation. **Ling Xia:** Conceptualization, Funding acquisition, Supervision. **Jiandong Mao:** Conceptualization, Funding acquisition.

Declaration of competing interest

The authors declare that they have no known competing financial or personal relationships that could be viewed as influencing the work reported in this paper.

Data availability statement

The datasets generated during and/or analyzed during the current study are available from the corresponding author on reasonable request.

Acknowledgements

The authors would like to appreciate all participants for data collection and providing constructive comments.

Appendix A. Supplementary material

Supplementary material related to this article can be found online at https://doi.org/10.1016/j.irbm.2023.100805.

References

[1] Camici PG, d'Amati G, Rimoldi O. Coronary microvascular dysfunction: mechanisms and functional assessment. Nat Rev Cardiol 2015;12:48–62. https://doi.org/10.1038/nrcardio.2014.160.
[2] Khan MA, Hashim MJ, Mustafa H, Baniyas MY, Al Suwaidi SKBM, AlKatheeri R, et al. Global epidemiology of ischemic heart disease: results from the global burden of disease study. Cureus 2020;12:e9349. https://doi.org/10.7759/cureus.9349.
[3] Kaski J-C, Crea F, Gersh BJ, Camici PG. Reappraisal of ischemic heart disease. Circulation 2018;138:1463–80. https://doi.org/10.1161/CIRCULATIONAHA.118.031373.
[4] Mangiacapra F, Viscusi MM, Verolino G, Paolucci L, Nusca A, Melfi R, et al. Invasive assessment of coronary microvascular function. J Clin Med 2021;11:228. https://doi.org/10.3390/jcm11010228.
[5] Marinescu Mark A, Löffler Adrián I, Ouellette Michelle, Smith Lavone, Kramer Christopher M, Bourque JM. Coronary microvascular dysfunction, microvascular angina, and treatment strategies. JACC Cardiovasc Imag 2015;8:210–20. https://doi.org/10.1016/j.jcmg.2014.12.008.
[6] Del Buono MG, Montone RA, Camilli M, Carbone S, Narula J, Lavie CJ, et al. Coronary microvascular dysfunction across the spectrum of cardiovascular diseases: JACC state-of-the-art review. J Am Coll Cardiol 2021;78:1352–71. https://doi.org/10.1016/j.jacc.2021.07.042.
[7] Herrmann J, Kaski JC, Lerman A. Coronary microvascular dysfunction in the clinical setting: from mystery to reality. Eur Heart J 2012;33:2771–83. https://doi.org/10.1093/eurheartj/ehs246.
[8] Sara JD, Widmer RJ, Matsuzawa Y, Lennon RJ, Lerman LO, Lerman A. Prevalence of coronary microvascular dysfunction among patients with chest pain and nonobstructive coronary artery disease. JACC: Cardiovasc Interv 2015;8:1445–53. https://doi.org/10.1016/j.jcin.2015.06.017.
[9] Martínez Pereyra V, Seitz A, Mahrholdt H, Bekeredjian R, Sechtem U, Ong P. Coronary microvascular dysfunction in patients with mild-to-moderate aortic stenosis - insights from intracoronary acetylcholine testing. Int J Cardiol Heart Vasc 2020;31:100658. https://doi.org/10.1016/j.ijcha.2020.100658.
[10] Ong P, Camici PG, Beltrame JF, Crea F, Shimokawa H, Sechtem U, et al. International standardization of diagnostic criteria for microvascular angina. Int J Cardiol 2018;250:16–20. https://doi.org/10.1016/j.ijcard.2017.08.068.
[11] Padro T, Manfrini O, Bugiardini R, Canty J, Cenko E, De Luca G, et al. ESC working group on coronary pathophysiology and microcirculation position paper on 'coronary microvascular dysfunction in cardiovascular disease'. Cardiovasc Res 2020;116:741–55. https://doi.org/10.1093/cvr/cvaa003.
[12] Liu H, Ou S, Liu P, Xu Y, Gong Y, Xia L, et al. Effect of microcirculatory resistance on coronary blood flow and instantaneous wave-free ratio: a computational study. Comput Methods Programs Biomed 2020;196:105632. https://doi.org/10.1016/j.cmpb.2020.105632.
[13] Geng Y, Wu X, Liu H, Zheng D, Xia L. Index of microcirculatory resistance: state-of-the-art and potential applications in computational simulation of coronary artery disease. J Zhejiang Univ Sci B 2022;23:123–40. https://doi.org/10.1631/jzus.B2100425.
[14] Sara JD, Sugrue A, Kremen V, Qiang B, Sapir Y, Attia ZI, et al. Electrocardiographic predictors of coronary microvascular dysfunction in patients with nonobstructive coronary artery disease: utility of a novel T wave analysis program. Int J Cardiol 2016;203:601–6. https://doi.org/10.1016/j.ijcard.2015.10.228.
[15] Fabris Enrico, Hof AWvt. 7- Angiography and electrocardiography (ECG) for the assessment of coronary microvascular obstruction. In: Niccoli G, Eitel I, editors. Coronary microvascular obstruction in acute myocardial infarction. Academic Press; 2018. p. 109–26.
[16] Ong P, Athanasiadis A, Hill S, Schäufele T, Mahrholdt H, Sechtem U. Coronary microvascular dysfunction assessed by intracoronary acetylcholine provocation testing is a frequent cause of ischemia and angina in patients with exercise-induced electrocardiographic changes and unobstructed coronary arteries. Clin Cardiol 2014;37:462–7. https://doi.org/10.1002/clc.22282.
[17] Dose N, Michelsen MM, Mygind ND, Pena A, Ellervik C, Hansen PR, et al. Ventricular repolarization alterations in women with angina pectoris and suspected coronary microvascular dysfunction. J Electrocardiol 2018;51:15–20. https://doi.org/10.1016/j.jelectrocard.2017.08.017.
[18] Zhou Z, Liu Y, Wang Z, Wang Y, Zhang J, Yang C. The value of standard deviation of normal RR Interval in predicting coronary microvascular dysfunction in patients with ischemia with non obstructive coronary arteries. Chin Circ J 2022;37:804–9. https://doi.org/10.3969/j.issn.1000-3614.2022.08.008.
[19] Sara JD, Lennon RJ, Ackerman MJ, Friedman PA, Noseworthy PA, Lerman A. Coronary microvascular dysfunction is associated with baseline QTc prolongation amongst patients with chest pain and non-obstructive coronary artery disease. J Electrocardiol 2016;49:87–93. https://doi.org/10.1016/j.jelectrocard.2015.10.006.
[20] Dehnavi AR, Farahabadi I, Rabbani H, Farahabadi A, Mahjoob MP, Dehnavi NR. Detection and classification of cardiac ischemia using vectorcardiogram signal via neural network. J Res Med Sci 2011;16:136–42.
[21] Khan SI, Pachori RB. Automated detection of posterior myocardial infarction from vectorcardiogram signals using Fourier–Bessel series expansion based empirical wavelet transform. IEEE Sens Lett 2021;5:1–4. https://doi.org/10.1109/LSENS.2021.3070142.
[22] Zhao X, Zhang J, Gong Y, Xu L, Liu H, Wei S, et al. Reliable detection of myocardial ischemia using machine learning based on temporal-spatial characteristics of electrocardiogram and vectorcardiogram. Front Physiol 2022. https://doi.org/10.3389/fphys.2022.854191.
[23] Deng M, Tang M, Wang C, Shan L, Zhang L, Zhang J, et al. Cardiodynamicsgram as a new diagnostic tool in coronary artery disease patients with nondiagnostic electrocardiograms. Am J Cardiol 2017;119:698–704. https://doi.org/10.1016/j.amjcard.2016.11.028.
[24] Perez Alday EA, Gu A, Shah AJ, Robichaux C, Ian Wong A-K, Liu C, et al. Classification of 12-lead ECGs: the PhysioNet/computing in cardiology challenge 2020. Physiol Meas 2021;41:124003. https://doi.org/10.1088/1361-6579/abc960.
[25] Ahn Jung-Min, Zimmermann Frederik M, Arora Satish, Solberg Ole-Geir, Angerås Oskar, Rolid Katrine, et al. Prognostic value of comprehensive intracoronary physiology assessment early after heart transplantation. Eur Heart J 2021;42:4918–29. https://doi.org/10.1093/eurheartj/ehab568.
[26] Khan SI, Pachori RB. Derived vectorcardiogram based automated detection of posterior myocardial infarction using FBSE-EWT technique. Biomed Signal Process Control 2021;70:103051. https://doi.org/10.1016/j.bspc.2021.103051.
[27] Grishman A, Borun ER, Jaffe HL. Spatial vectorcardiography: technique for the simultaneous recording of the frontal, sagittal, and horizontal projections. Am Heart J 1951;41:483–93. https://doi.org/10.1016/0002-8703(51)90017-8.
[28] Qaisar Saeed Mian, Khan SI, Dallet Dominique, Tadeusiewicz Ryszard, Pławiak Paweł. Signal-piloted processing metaheuristic optimization and wavelet decomposition based elucidation of arrhythmia for mobile healthcare. Biocybern Biomed Eng 2022;42:681–94. https://doi.org/10.1016/j.bbe.2022.05.006.
[29] Kors JA, Van Herpen G, Sittig AC, Van Bemmel JH. Reconstruction of the Frank vectorcardiogram from standard electrocardiographic leads: diagnostic comparison of different methods. Eur Heart J 1990;11:1083–92. https://doi.org/10.1093/oxfordjournals.eurheartj.a059647.
[30] Song J, Yan H, Xiao Z, Yang X, Zhang X. A robust and efficientalgorithm for ST–T complex detection in electrocardiograms. J Mech Med Biol 2012;11:1103–11. https://doi.org/10.1142/s0219519411004198.
[31] Haq AU, Li J, Memon MH, Hunain Memon M, Khan J, Marium SM. Heart disease prediction system using model of machine learning and sequential backward selection algorithm for features selection. In: 2019 IEEE 5th international conference for convergence in technology (I2CT); 2019. p. 1–4.
[32] Sotiropoulos DN, Tsihrintzis GA. Artificial immune system-based classification in class-imbalanced problems. In: 2011 IEEE workshop on evolving and adaptive intelligent systems (EAIS); 2011. p. 131–8.
[33] Japkowicz N, Stephen S. The class imbalance problem: a systematic study. IOS Press 2002;6:429–49. https://doi.org/10.3233/IDA-2002-6504.
[34] Lemnaru C, Potolea R. Imbalanced classification problems: systematic study, issues and best practices. In: Zhang R, Zhang J, Zhang Z, Filipe J, Cordeiro J, editors. Enterprise information systems. Berlin, Heidelberg: Springer Berlin Heidelberg; 2012. p. 35–50.
[35] Doukim CA, Dargham JA, Chekima A. Finding the number of hidden neurons for an MLP neural network using coarse to fine search technique. In: 10th international conference on information science, signal processing and their applications (ISSPA 2010); 2010. p. 606–9.
[36] Qi S, Zhao W, Chen Y, Chen W, Li J, Zhao H, et al. Comparison of machine learning approaches for radioisotope identification using NaI(TI) gamma-ray spectrum. Appl Radiat Isot 2022;186:110212. https://doi.org/10.1016/j.apradiso.2022.110212.
[37] Al Bataineh A, Manacek S. MLP-PSO hybrid algorithm for heart disease prediction. J Person Med 2022;12:1208. https://doi.org/10.3390/jpm12081208.
[38] Zeng X, Yeung DS. Hidden neuron pruning of multilayer perceptrons using a quantified sensitivity measure. Neurocomputing 2006;69:825–37. https://doi.org/10.1016/j.neucom.2005.04.010.
[39] Itano F, Sousa M, Del-Moral-Hernandez E. Extending MLP ANN hyper-parameters optimization by using genetic algorithm. In: 2018 international joint conference on neural networks (IJCNN). Rio de Janeiro, Brazil: IEEE; 2018.

[40] Assunção F, Lourenço N, Machado P, Ribeiro B. Automatic generation of neural networks with structured grammatical evolution. In: 2017 IEEE congress on evolutionary computation (CEC); 2017. p. 1557–64.
[41] Xue J, Shen B. A novel swarm intelligence optimization approach: sparrow search algorithm. Syst Sci Control Eng 2020;8:22–34. https://doi.org/10.1080/21642583.2019.1708830.
[42] Gálvez J, Cuevas E, Becerra H, Avalos O. A hybrid optimization approach based on clustering and chaotic sequences. Int J Mach Learn Cybern 2020;11:359–401. https://doi.org/10.1007/s13042-019-00979-6.
[43] Wang Y. Image scrambling method based on chaotic sequences and mapping. In: 2009 first international workshop on education technology and computer science; 2009. p. 453–7.
[44] Liu G, Shu C, Liang Z, Peng B, Cheng L. A modified sparrow search algorithm with application in 3d route planning for UAV. Sensors 2021;21:1224. https://doi.org/10.3390/s21041224.
[45] Lyu X, Mu X, Zhang J, Zheng W. Chaos sparrow search optimization algorithm. J Beijing Univ Aeronaut Astronaut 2021;47:1712–20. https://doi.org/10.13700/j.bh.1001-5965.2020.0298.
[46] Yu Y, Gao SC, Cheng S, Wang YR, Song SY, Yuan FG. CBSO: a memetic brain storm optimization with chaotic local search. Memet Comp 2018;10:353–67. https://doi.org/10.1007/s12293-017-0247-0.
[47] Li L, Sui X, Lian J, Yu F, Zhou Y. Vehicle interaction behavior prediction with self-attention. Sensors 2022;22:429. https://doi.org/10.3390/s22020429.
[48] Lodhi A, Qureshi A, Sharif U, Ashiq Z. A novel approach using voting from ECG leads to detect myocardial infarction. In: Proceedings of the 2018 intelligent systems conference (IntelliSys), vol. 2. 2019. p. 337–52.
[49] Khan SI, Pachori RB. Automated classification of lung sound signals based on empirical mode decomposition. Expert Syst Appl 2021;184:115456. https://doi.org/10.1016/j.eswa.2021.115456.
[50] Zhao H, Zhang X, Xu Y, Gao L, Ma Z, Sun Y, et al. Predicting the risk of hypertension based on several easy-to-collect risk factors: a machine learning method. Front Public Health 2021;9:619429. https://doi.org/10.3389/fpubh.2021.619429.
[51] Mian Qaisar S, Khan SI, Srinivasan K, Krichen M. Arrhythmia classification using multirate processing metaheuristic optimization and variational mode decomposition. J King Saud Univ, Comput Inf Sci 2023;35:26–37. https://doi.org/10.1016/j.jksuci.2022.05.009.
[52] Khan SI, Qaisar SM, Pachori RB. Automated classification of valvular heart diseases using FBSE-EWT and PSR based geometrical features. Biomed Signal Process Control 2022;73:103445. https://doi.org/10.1016/j.bspc.2021.103445.
[53] Khan SI, Choubey SB, Choubey A, Bhatt A, Naishadhkumar PV, Basha MM. Automated glaucoma detection from fundus images using wavelet-based denoising and machine learning. Concurr Eng 2022;30:103–15. https://doi.org/10.1177/1063293X211026620.
[54] Alizadehsani R, Abdar M, Roshanzamir M, Khosravi A, Kebria PM, Khozeimeh F, et al. Machine learning-based coronary artery disease diagnosis: a comprehensive review. Comput Biol Med 2019:111. https://doi.org/10.1016/j.compbiomed.2019.103346.
[55] Hasan MA, Abbott D. A review of beat-to-beat vectorcardiographic (VCG) parameters for analyzing repolarization variability in ECG signals. Biomed Tech 2016;61:3–17. https://doi.org/10.1515/bmt-2015-0005.
[56] Correa RÏ, Arini PD, Correa LS, Valentinuzzi M, Laciar E. Novel technique for ST-T interval characterization in patients with acute myocardial ischemia. Comput Biol Med 2014;50:49–55. https://doi.org/10.1016/j.compbiomed.2014.04.009.
[57] Cato ter Haar C, Maan Arie C, Warren Stafford G, Ringborn Michael, Milan Horáček B, Schalij Martin J, et al. Difference vectors to describe dynamics of the ST segment and the ventricular gradient in acute ischemia. J Electrocardiol 2013;46:302–11. https://doi.org/10.1016/j.jelectrocard.2013.04.004.
[58] Feeny A, Tereshchenko LG. Beat-to-beat determinants of the beat-to-beat temporal and spatial variability of repolarization. J Electrocardiol 2016;49:417–22. https://doi.org/10.1016/j.jelectrocard.2016.01.007.
[59] Sun Q, Wang L, Wang C, Wang Q, Wu W, Zhao Y, et al. Early detection of myocardial ischemia based on deterministic learning and cardiodynamicsgram. Acta Autom Sin 2020;46:1908–26. https://doi.org/10.16383/j.aas.c190899.
[60] Artiles José AP, Chaves Daniel PB, Pimentel Cecilio. Image encryption using block cipher and chaotic sequences. Signal Process Image Commun 2019;79:24–31. https://doi.org/10.1016/j.image.2019.08.014.
[61] Wang P, Zhang Y, Yang H. Research on economic optimization of microgrid cluster based on chaos sparrow search algorithm. Comput Intell Neurosci 2021;2021:5556780. https://doi.org/10.1155/2021/5556780.
[62] Zhang X, Xiao F, Tong X, Yun J, Liu Y, Sun Y, et al. Time optimal trajectory planing based on improved sparrow search algorithm. Front Bioeng Biotechnol 2022;10:1–14. https://doi.org/10.3389/fbioe.2022.852408.
[63] Sun G, Lan Y, Zhao R. Differential evolution with Gaussian mutation and dynamic parameter adjustment. Soft Comput 2019;23:1615–42. https://doi.org/10.1007/s00500-017-2885-z.
[64] Rudolph G. Local convergence rates of simple evolutionary algorithms with Cauchy mutations. IEEE Trans Neural Netw 1997;1:249–58. https://doi.org/10.1109/4235.687885.
[65] Wang Y, Liu Q, Sun J, Wang L, Song X, Zhao X. Multistrategy improved sparrow search algorithm optimized deep neural network for esophageal cancer. Comput Intell Neurosci 2022;2022:1036913. https://doi.org/10.1155/2022/1036913.
[66] Zhang J, Ma M, Li H, Pu Z, Liu H, Huang T, et al. Early diagnosis of coronary microvascular dysfunction by myocardial contrast stress echocardiography. Math Biosci Eng 2023;20:7845–58. https://doi.org/10.3934/mbe.2023339.